A phase-field model for the magnetic shape memory effect

C. MENNERICH, F. WENDLER, M. JAINTA, B. NESTLER

Institute of Materials and Processes
Karlsruhe University of Applied Sciences
Moltkestraße 30, 76133 Karlsruhe, Germany
e-mail: Christian.Mennerich@hs-karlsruhe.de
Frank.Wendler@hs-karlsruhe.de

THE MAGNETIC SHAPE MEMORY EFFECT, that is the rearrangement of martensitic microstructure induced by an external magnetic field, is of interest in many fields of application. The effect is based on a preceding martensitic transformation and provides a giant macroscopic strain. This change in length is induced by the complex interplay of magnetic and elastic energies. The effective free energy functional describing this effect is derived and employed in a phase-field model. The coupled equations of motion for the phase fields, the elastic displacement field and the spontaneous magnetization, follow on the energy minimizing principles. Numerical simulations with parameters reflecting the Ni_2MnGa material system show the general applicability of the aproach.

Key words: magnetic shape memory effect, phase-field modeling, twin boundary motion.

1. Introduction

DURING THE LAST DECADE, magnetic shape memory alloys (MSMAs) have attained major interest. Providing fast response rates and low energetic costs in operation, they are well suited as components for which great changes in length are required (e.g. as components in actuators or dampers). The large observed strain is based on the magnetic shape memory effect (MSME), that is the rearrangement of microstructure induced by an applied magnetic field, and depends on the crystal structure of the MSMA. Since the first observation of the MSME in 1996 by ULLAKKO *et al.* [1], in single crystals at room temperature, changes in length by more than six percent in five-layered tetragonal (see [2]) and almost ten percent in seven-layered orthorhombic (see [3]) Ni_2MnGa alloys, have been observed. Contrary to the conventional thermoelastic shape memory effect that is based on a reversible martensitic transformation (MT) from a high temperature austenite phase into a lower temperature martensite phase and back again (see [4]), the MSME is entirely settled in the martensitic state of the ma-

terial (see [5]). As MSMAs are ferromagnetic hard materials, they provide a high magneto-crystalline anisotropy. The application of an external magnetic field induces the rearrangement of the martensitic variants in the microstructure and causes a macroscopic length change. ENTEL *et al.* review the MSME and properties of MSMAs in [6]. One major factor determining the MSME is the transformation strain caused by the transition from the austenite to the martensite, that depends on the change in the lattice constants. Hence, the composition of the alloy Ni_2MnGa is varied to optimize the material properties. Because the magnetic properties may change synchronously, a systematical, purely experimental approach is extremely time-consuming. Simulations of dynamic microstructure response under different material properties and physical stress and field states may help to find faster improvements and reveal new kinetic pathways, not taken into account so far.

The paper at hand is organized as follows. We first give a short review of the MSME and its prerequisites that enter our modeling approach in Sec. 2. This is the MT, with focus on the cubic-to-tetragonal MT appearing in Ni_2MnGa, and the possible symmetrically equivalent twin variants. In Sec. 3, we give a very brief overview of the existing phase-field models for the MSME. After that, the phase-field approach for our MSME model is described. We derive the constituting free energy functional and give the equations of motion that drive the system evolution. A brief summary of the numerical treatment of the model implementation is given. Special techniques to handle the demagnetization energy are necessary, as it is one of the most severe limiting factors for our simulations because of its computational complexity. Sec. 4 shows the results of numerical simulations and interprets them. The scaling relations between physical parameters (reflecting five-layered tetragonal Ni_2MnGa) and the dimensionless simulation parameters are given. The final Sec. 5 briefly discusses the achieved results and gives an outlook for our future work in the field of phase-field MSME modeling.

2. The magnetic shape memory effect

In this section we state the most important prerequisites used in our modeling approach as well as a brief review of the basic principle of the MSME, i.e. the foregoing martensitic transformation and the rearrangement of the martensitic microstructure induced by the application of an external applied magnetic field.

2.1. Prerequisites

For magnetic shape memory materials that are to be used as actuators or dampers operated at constant temperature T_{op}, we make the following necessary assumptions. First, the operation temperature has to be below the Curie temper-

ature T_{Curie} and the martensitic start temperature T_{ms} (i.e. $T_{\mathrm{op}} < T_{\mathrm{Curie}}, T_{\mathrm{ms}}$). Second, any external applied magnetic field is constant over (sufficiently long periods of) time. Third, the material under consideration should be ferromagnetic hard and homogeneous in the sense that the concentration is the same everywhere in the material (as it is the case in Heussler alloys like Ni_2MnGa). The concept of material symmetry reflects the fact that physical properties are the same in equivalent crystallographic directions. We assume small strains, so the Lagrangian strain tensor can be linearized. As the operation of inversion is unphysical, we restrict the notion of point groups to proper rotations. Detailed explanation of these concepts can be found in the instructive articles of BHATTACHARYA [7] and DESIMONE and JAMES [8], that we follow in this section.

2.2. The MT and the MSME

Preceding the MSME is a MT, that is a first-order diffusionless, displacive and shear-like phase transition. The MT starts from a high temperature austenite parent phase and results in a lower temperature martensite product phase (see e.g. [4]). Usually, this transformation leads to a loss of crystallographic symmetry (even if, in principle, the gain of symmetry is possible). Starting in the high temperature state, upon cooling, the Bravais lattice of the austenite deforms to the Bravais lattice of the martensite. The material is then strained with respect to the parent phase. The deformation strains are the so-called Bain strains and are described by transformation matrices. Assuming that the point group of the martensite $\mathcal{P}_m$ is a proper subgroup of the point group $\mathcal{P}_a$ of the austenite, there are $|\mathcal{P}_a|/|\mathcal{P}_m|$ different deformation variants possible, and the deformations describing the different variants are related to each other via the group theoretic operation of conjugation with elements of $\mathcal{P}_a$ (see e.g. [9]). All variants are energetically and crystallographically equivalent (due to the assumption of material symmetry). This results in a well-defined energy landscape with energy wells at the austenite and martensite deformation. When the material is at a temperature below the martensitic start temperature T_{ms}, the martensite wells are energetically lower than those of the austenite (cf. Fig. 1a). The orientation relation between the martensitic variants is not arbitrary, but also well defined. Since all variants develop from the same parent phase, the deformations, as we assume in linear elasticity, obey the rank one kinematic compatibility condition (see [7])

$$(2.1) \qquad \mathbf{U}_i - \mathbf{U}_j = \frac{1}{2} \left(\mathbf{a} \otimes \mathbf{n} + \mathbf{n} \otimes \mathbf{a} \right).$$

In this condition, $\mathbf{U}_i$ and $\mathbf{U}_j$ are Bain matrices, $\mathbf{n}$ is the normal to the plane separating the variants i and j, and $\mathbf{a}$ is a simple shear. From Eq. (2.1) one
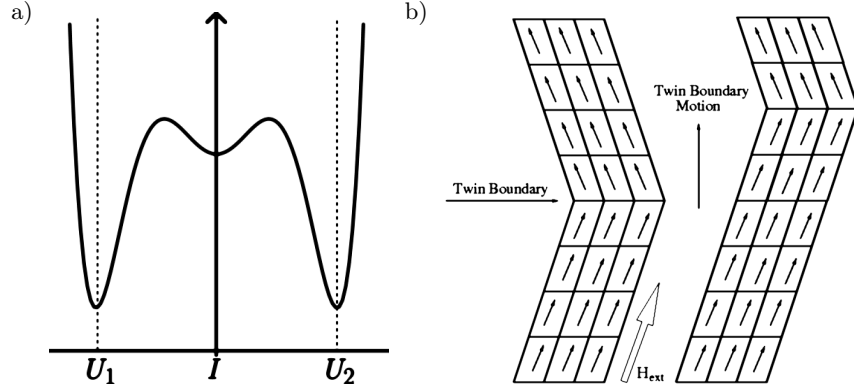
Fig. 1. a) The energy landscape of a material at a temperature $T < T_{\mathrm{ms}}$ as a function of deformation from the austenite parent phase: equivalent global minima exist for two possible martensitic variants. b) The basic principle of the motion of twin variants induced by an applied magnetic field in MSME materials.

obtains that the variants are twins, and the possible twinnig modes and directions can be derived from the linear theory presented in [7]. This equation is therefore called 'twinning equation'. We look now at the cubic-to-tetragonal MT (cf. Fig. 2) that is occuring in Ni_2MnGa: the point group of the cubic parent phase consists of 24 rotations, while in the point group of the tetragonal martensite product phase only eight rotations are left, so three different variants are possible. The occuring Bain matrices are

$$(2.2) \quad \mathbf{U}_1 = \begin{pmatrix} \beta & 0 & 0 \\ 0 & \alpha & 0 \\ 0 & 0 & \alpha \end{pmatrix}, \quad \mathbf{U}_2 = \begin{pmatrix} \alpha & 0 & 0 \\ 0 & \beta & 0 \\ 0 & 0 & \alpha \end{pmatrix}, \quad \mathbf{U}_3 = \begin{pmatrix} \alpha & 0 & 0 \\ 0 & \alpha & 0 \\ 0 & 0 & \beta \end{pmatrix},$$

where α and β are related to the strains, following from the deformations of the crystal axes. Twinning takes place along the $(110)_c$ directions (referred to in the cubic system).

All three possible pairs of variants can form a twin boundary (i.e. for all $i \neq j \in \{1, 2, 3\}$ exists a solution to Eq. (2.1)). The angle of rotation between the shortened c-axes of two variants in Ni_2MnGa is about $86.5°$ (cf. [10]). If the twinned martensitic material is additionally a hard ferromagnetic, it is energetically more favorable to rearrange the twinned microstructure than to pull local magnetic moments out of the magnetically preferred directions (the so-called easy axes). This is the basic principle of the MSME. The application of an external magnetic field increases the magnetostatic Zeeman energy in the system, and the principle of energy minimization leads to the alignment of magnetic moments parallel to the direction of the external field. If now the external field privileges one of the martensitic variants, it grows on the expense of the other variants.
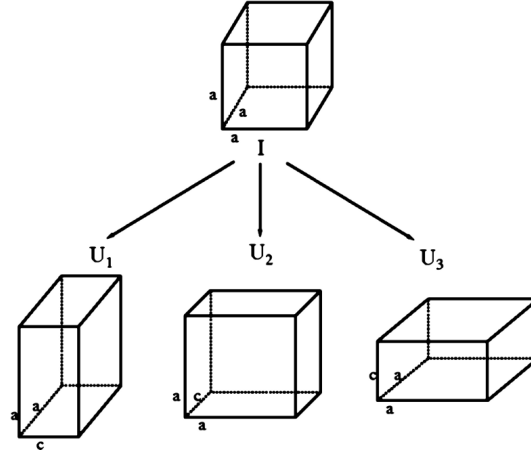
Fig. 2. The MT in Ni_2MnGa: Transformation from a cubic austenite parent phase to a tetragonal product phase by shortening a cubic axis. Three crystallograpically and energetically equivalent variants are possible, described by the Bain matrices $\mathbf{U}_1, \mathbf{U}_2$ and $\mathbf{U}_3$. The matrix $\mathbf{I}$ is the 3×3 identity matrix, representing the austenite state.

The rearrangement process comes along with macroscopic strains, depending on the geometry of the specimen. The functional principle of the MSME is sketched in Fig. 1b.

3. A phase field model for the MSME

In this section, the phase-field model on which our modeling approach is based, is introduced. Since in the last years several phase-field models for the MSME were proposed in the literature, we give a very brief review of the, to our knowledge, most frequently cited ones: the models discussed by ZHANG and CHEN ([11, 12]), JIN ([13]) and LI *et al.* ([14, 15]). For more detailed explanations see these works and the references therein. Characteristic for every phase-field model is the choice of a continuous order parameter $\mathbf{\Phi}$, that describes the state of the system under consideration. The interplay of a gradient energy $\propto |\nabla\mathbf{\Phi}|^2$ and a potential energy term that reflects the energy landscape of the physical system, are responsible for the establishment of a diffusive interface of definite width. In the case of the MSME, different choices for the order parameter are possible.

The phase-field models in [11] and [13] use a long range order parameter related to the stress-free strains (or eigenstrains) of different martensitic variants. The potential energy is constructed from the Landau theory of phase transitions by approximation of the Landau polynomial in terms of the order parameter. Thus, the symmetry relation between the martensitic variants and the cubic parent phase are reflected. The coefficients of the polynomial have to be very

well chosen to reflect the material properties. To avoid these difficulties, the order parameter used by LI *et al.* [15] is based on the local volume fractions of the martensitic variants. From these, a reduced order parameter $\boldsymbol{\mu} = (\mu_1, \mu_2)$ is derived that is equivalent to the long-range order parameter of stress-free strain. This is done by relating $\boldsymbol{\mu}$ to a multi-rank lamination that is a proven minimizer of the magneto-elastic free energy (see [7, 8]). The proposed potential reflects the multi-well energy landscape and penalizes deviations from the wells proportional to the magnetocrystalline anisotropy constant.

The approach presented in this paper is based on the multi phase-field model of NESTLER *et al.* [16], and is consequently derived by interpolation of bulk-free energies. The order parameters here are identical to the local volume fractions of the martensitic variants, where the variants energy landscape is reflected in the elastic part of the free energy. The used multi-obstacle potential is chosen to penalize the purely interfacial states. In opposition to the other models, no mechanical equilibrium is assumed, as the elastic transitions may happen with nearly the speed of sound (see e.g. [17, Chap. 2]), i. e. on a time scale comparable to the one on which the reorganisation of magnetic moments takes place.

In the following subsections, we state the micromagnetic and elastic energy contributions that are necessary to model the MSME, and give the equations of motion that describe the time-spatial evolution of the system. The latter are derived from variational calculus and follow the principle of minimizing the free energy in the system.

3.1. The adopted multi-phase-field model

To treat the arising boundary value problem, the phase-field model introduced in [16] is applied. In general, this method allows the modeling of multi-phase multi-component systems, consisting of N phases and K components in a region $\Omega \subseteq \mathbb{R}^3$, and the description of its time-spatial evolution. One general advantage of the phase-field method is the avoidance of explicit front tracking. This is achieved by introducing a set of non-conserved, smooth order parameters with values in the closed interval $[0, 1]$, the so-called phase fields. They are collected in the order parameter $\boldsymbol{\phi} = (\phi_1, \dots, \phi_N)$. The bulk of a phase $\alpha \in \{1, \dots, N\}$ is defined as the preimage $\phi_\alpha^{-1}(\{1\})$, and a diffusive interface separates different phases. The diffusive interface is the area where $\alpha \leq N$ exists with $\phi_\alpha \in \,]0, 1[$. All state variables depend on space and time, so their common domain is $\Omega \times \mathbb{R}_{\geq 0}$. The general integral Helmholtz free energy formulation is of Ginzburg–Landau type:

$$(3.1) \qquad \mathcal{F}(\boldsymbol{\phi}, \dots) = \int_\Omega \left(\xi a(\boldsymbol{\phi}, \nabla \boldsymbol{\phi}) + \frac{1}{\xi} w(\boldsymbol{\phi}) + f(\boldsymbol{\phi}, \dots) \right) dx.$$

The integral expression may depend on all thermodynamic variables in the system. The first two addends in Eq. (3.1) are surface energy contributions responsible for the establishment of the diffusive interface of finite thickness (see [18]). Via the length parameter $\xi \in \mathbb{R}_{>0}$, the interface width can be adjusted. The function $a(\boldsymbol{\phi}, \nabla\boldsymbol{\phi})$ is a gradient energy that broadens the interface, while $w(\boldsymbol{\phi})$ is a potential that penalizes the interfacial states. This potential is non-convex, providing N global minima corresponding to the bulk states of each phase. For $w(\boldsymbol{\phi})$, a higher-order variant of a multi-obstacle potential is used, that allows to suppress the occurrence of spurious 'third phases' in binary interfaces ([16]). The bulk free energy $f(\boldsymbol{\phi}, \dots)$ may depend on several physical quantities and is the interpolation of individual bulk free energies $f^\alpha(\dots)$, defined for every phase α, and in a general context reads as

$$(3.2) \qquad f(\boldsymbol{\phi}, \dots) = \sum_{\alpha=1}^{N} h(\phi_\alpha) f^\alpha(\dots).$$

The used interpolation function $h : [0,1] \rightarrow [0,1]$ has to be continuously differentiable and to satisfy the conditions $h(0) = 0$ and $h(1) = 1$. We chose $h(x) = x^2(3 - 2x)$ in our model.

3.2. Magnetoelastic free energies

A general theory of micromagnetics goes back to the works of BROWN (see [19]). We consider the magnetization in a ferromagnetic body $\Omega \subseteq \mathbb{R}^3$. The magnetization is described by the time- and space-dependent vector field of spontaneous magnetization $\mathbf{M}$. As a consequence of our assumptions (cf. Sec. 2.1), we have $|\mathbf{M}(x,t)| \equiv M_S \in \mathbb{R}_{>0}$ for all $x \in \Omega$ and $t \in \mathbb{R}_{\geq 0}$ (where M_S is the saturation magnetization). We therefore restrict our considerations to a unit vector field $\mathbf{m} \equiv \frac{1}{M_S}\mathbf{M}$ that evolves point-wise on the unit sphere

$$\mathbb{S}^2 = \{x \in \mathbb{R}^3 \mid |x| = 1\}.$$

Linear elasticity is described in terms of the so-called displacement field $\mathbf{u}$. For each point $x \in \Omega$ and every time $t \in \mathbb{R}_{\geq 0}$, the deviation of x from its initial position is given by $\mathbf{u}(x,t)$. The elastic strain ϵ in the system is a function of the displacement field:

$$(3.3) \qquad \epsilon(\mathbf{u}) = \frac{1}{2}(\nabla\mathbf{u} + \nabla\mathbf{u}^T).$$

For a good brief review on the basics of continuum mechanics, we refer to the book of Phillips [20, Chapter 2]. As micromagnetic and elastic state variables in the system we get the (normalized) vector field of spontaneous magnetization

$$\mathbf{m} : \Omega \times \mathbb{R}_{\geq 0} \rightarrow \mathbb{S}^2, \qquad (x,t) \mapsto \mathbf{m}(x,t) = (m_1(x,t), m_2(x,t), m_3(x,t))^T$$

and the displacement field

$$\mathbf{u} : \Omega \times \mathbb{R}_{\geq 0} \to \mathbb{R}^3, \qquad (x,t) \mapsto \mathbf{u}(x,t) = (u_1(x,t), u_2(x,t), u_3(x,t))^T.$$

The free energy density of interest consists of five micromagnetic and magneto-elastic energy contributions (cf. [21]), namely the Zeeman (or external) energy, the demagnetization energy, the exchange energy, the magneto-crystalline anisotropy energy and the magneto-elastic energy:

$$(3.4) \qquad f(\boldsymbol{\phi}, \mathbf{u}, \mathbf{m}) = f_{\text{ext}}(\mathbf{m}) + f_{\text{demag}}(\mathbf{m}) + f_{\text{exch}}(\mathbf{m})$$

$$+ f_{\text{aniso}}(\boldsymbol{\phi}, \mathbf{m}) + f_{\text{m-el}}(\boldsymbol{\phi}, \mathbf{u}, \mathbf{m}).$$

The first two energies in Eq. (3.4) have a magnetostatic character. For contributions depending on a variant α, the interpolation approach Eq. (3.2) is applied. We now briefly discuss these energy densities (see e.g. [21] or [22] for more detailed explanations). The micromagnetic permeability in the vacuum $\mu_0 = 4\pi \cdot 10^{-7} \frac{H}{m}$ (a fundamental constant) and the saturation magnetization M_S are frequently used here.

The magnetostatic Zeeman energy describes the interaction of the local magnetization $\mathbf{m}$ with an applied external magnetic field $\mathbf{H}_{\text{ext}}$:

$$f_{\text{ext}}(\mathbf{m}) = -\mu_0 M_S (\mathbf{H}_{\text{ext}} \cdot \mathbf{m}).$$

The demagnetization energy (or magnetostatic self-energy) is a long-range energy. It accounts for the interactions between all local magnetic moments in the system:

$$f_{\text{demag}}(\mathbf{m}) = -\frac{1}{2}\mu_0 M_S (\mathbf{H}_{\text{demag}} \cdot \mathbf{m}).$$

The demagnetization field $\mathbf{H}_{\text{demag}}$ is derived from Maxwell's equations. It is a curl-free field (see [8]), and from the Helmholtz decomposition theorem follows the existence of a scalar potential $\psi : \mathbb{R}^3 \to \mathbb{R}$ such that $\mathbf{H}_{\text{demag}} = -\nabla\psi$, where the potential $\psi : \mathbb{R}^3 \to \mathbb{R}$ is the solution of the Poisson-type equation $\Delta\psi = -M_S(\nabla \cdot \mathbf{m})$, under suitable boundary conditions applied to the topological surface $\partial\Omega$ of the domain Ω (see e.g. [23] or [24]). A solution of $\mathbf{H}_{\text{demag}}$ can be derived in analogy to the potential in classical electrodynamics and consists, in the case of finitely extended material samples, of contributions from the region Ω and the surface $\partial\Omega$. In this case

$$\psi(r) = -M_S \int_{\Omega} \frac{1}{|r-r'|} \nabla \cdot \mathbf{m}(r') \, d^3r' + M_S \int_{\partial\Omega} \frac{1}{|r-r'|} \mathbf{n}(r') \cdot \mathbf{m}(r') \, d^2r'$$

is a solution for the scalar potential (cf. [25]). The field $\mathbf{H}_{\text{demag}}$ can be written explicitly as (see [24])

$$\mathbf{H}_{\text{demag}}(r) = -\frac{1}{4\pi} M_S \int\limits_{\Omega} \nabla \cdot \mathbf{m}(r') \frac{r - r'}{|r - r'|^3} \, d^3 r'$$

$$+ \frac{1}{4\pi} M_S \int\limits_{\partial\Omega} \mathbf{n}(r') \cdot \mathbf{m}(r') \frac{r - r'}{|r - r'|^3} \, d^2 r',$$

where $\mathbf{n}$ is a vector normal to $\partial\Omega$ pointing outwards. In the case of infinitely extended crystals the surface term in $\mathbf{H}_{\text{demag}}$ vanishes, but the solution stays valid. The demagnetization field depends on the local state of the magnetization $\mathbf{m}$, what makes the calculation of $\mathbf{H}_{\text{demag}}$ computationally complex. To gain efficient calculation methods, special assumptions to $\mathbf{m}$ and its discretization are applied (see Sec. 3.4).

The short-range dipole interactions of magnetic moments are described by the quantum mechanical exchange energy. It is expressed as the gradient square term

$$f_{\text{exch}}(\mathbf{m}) = A_{\text{exch}} |\nabla \mathbf{m}|^2.$$

Here, A_{exch} is the material-dependent exchange stiffness constant. In a more general context, this energy can be made variant dependent (cf. Eq. (3.2)).

The magneto-crystalline anisotropy takes the dependence of the local magnetization on the directions of preferred magnetization into account. The easy axes of local martensitic variants point in different directions, so this energy depends on the relative orientation of $\mathbf{m}$ and the easy axis. We here restrict to the uniaxial case having exactly one easy axis per variant. The energy density of variant α can be formulated as

$$f_{\text{aniso}}^{\alpha}(\boldsymbol{\phi}, \mathbf{m}) = K_{\text{aniso}} \left(1 - (\mathbf{m} \cdot \mathbf{p}^{\alpha})^2 \right),$$

where K_{aniso} is a material-dependent anisotropy constant, and $\mathbf{p}^{\alpha} \in \mathbb{S}^2$ is the direction of the easy axis of variant α. A general polynomial expression using even exponents of $(\mathbf{m} \cdot \mathbf{p}^{\alpha})$ to model anisotropy for different crystal systems is given in [22].

The coupling of micromagnetics and elasticity is realized by considering elastic energies as well as the stress-free strain (or eigenstrain) contributions. We assume small strains and the validity of Hooke's law of elasticity:

$$f_{\text{m-el}}^{\alpha}(\mathbf{u}, \mathbf{m}) = \frac{1}{2} \left((\epsilon(\mathbf{u}) - \epsilon_0^{\alpha}(\mathbf{m})) : \mathcal{C}^{\alpha}(\epsilon(\mathbf{u}) - \epsilon_0^{\alpha}(\mathbf{m})) \right).$$

Here, $\mathcal{C}^{\alpha}$ is the fourth-order variant dependent elastic property tensor and $\epsilon(\mathbf{u})$ is the second-order tensor of total strain (cf. Eq. (3.3)), depending on the displacement field. The total strain has to be adjusted by the stress-free strains from

martensitic variants which are interacting with local magnetizations. $\epsilon_0^\alpha(\mathbf{m})$ can be separated into two parts (see [13]):

$$(3.5) \qquad \epsilon_0^\alpha(\mathbf{m}) = \epsilon_0^{tr,\alpha} + \epsilon_0^{m,\alpha}(\mathbf{m}).$$

The first part is the variant-dependent transformation strain, the second is the magnetostrictive part. Assuming a cubic-to-tetragonal MT, we get as the transformation strain

$$\epsilon_0^{tr,\alpha} = \frac{a_t - a_c}{a_c}\mathbf{I} + \frac{c_t - a_c}{a_c}\mathbf{p}^\alpha \otimes \mathbf{p}^\alpha.$$

The expression originates from the MT and depends on the easy axis variants and the lattice constants of the cubic parent phase (a_c) and tetragonal product phase (a_t, c_t). This strain corresponds to the Bain strain. The magnetostrictive part reads in general (see [26])

$$\epsilon_0^{m,\alpha}(\boldsymbol{\phi}, \mathbf{m}) = \mathcal{N}^\alpha(\mathbf{m} \otimes \mathbf{m}).$$

Here, $\mathcal{N}^\alpha$ denotes the fourth-order magnetostrictive property tensor. As the magnetostrictive part is of minor influence in Ni$_2$MnGa (cf. [27]), it is neglected in this present work.

3.3. The MSME phase-field model and equations of motion

The complete free energy functional of the MSME phase-field model takes the form

$$(3.6) \qquad \mathcal{F}(\boldsymbol{\phi}, \mathbf{u}, \mathbf{m}) = \int_\Omega \left(\xi(\boldsymbol{\phi}, \nabla\boldsymbol{\phi}) + \frac{1}{\xi}w(\boldsymbol{\phi}) + f(\boldsymbol{\phi}, \mathbf{u}, \mathbf{m}) \right) dx,$$

where $f(\boldsymbol{\phi}, \mathbf{u}, \mathbf{m})$ is the free energy density from Eq. (3.4) and for each martensitic variant, an individual phase field is used. We remark here that for vanishing stress-free strain ($\epsilon_0^\alpha(\mathbf{m}) \equiv 0$), the pure elastic part of the model is the phase-field model previously given in [28]. The time-spatial evolution of the microstructure is described by a system of coupled partial differential equations. The evolving quantities are the order parameters $\boldsymbol{\phi} = (\phi_1, \ldots, \phi_N)$, the elastic displacement field $\mathbf{u}$ and the spontaneous magnetization $\mathbf{m}$. In general, the concept of minimizing the free energy in the system is applied.

As the values of the phase-fields represent the local volume fractions of the phases, an additional conservation constraint of the form

$$(3.7) \qquad \sum_{\alpha=1}^{N} \phi_\alpha \equiv 1$$

arises for the order parameter $\boldsymbol{\phi}$, always and everywhere in Ω. We adopt the widely used 'comma notation' for partial derivatives (i.e. for a function H depending on a variable X we define $H_{,X} := \frac{\partial}{\partial X} H$). By application of the Euler–Lagrange formalism from variational calculus, the equations of motion for the phase fields ϕ_α ($\alpha = 1, \ldots, N$) become (see [16])

$$
\begin{aligned}
(3.8) \qquad \tau \xi \frac{\partial \phi_\alpha}{\partial t} &= -\frac{\delta \mathcal{F}}{\delta \phi_\alpha} - \lambda = \frac{\delta}{\delta \phi_\alpha} \left(\int_\Omega \mathcal{L} \, dx \right) - \lambda \\
&= \left(\nabla \cdot \frac{\partial \mathcal{L}}{\partial \nabla \phi_\alpha} - \frac{\partial \mathcal{L}}{\partial \phi_\alpha} \right) - \lambda \\
&= \xi (\nabla \cdot a_{,\nabla \phi_\alpha}(\boldsymbol{\phi}, \nabla \boldsymbol{\phi}) - a_{,\phi_\alpha}(\boldsymbol{\phi}, \nabla \boldsymbol{\phi})) \\
&\quad - \frac{1}{\xi} w_{,\phi_\alpha}(\boldsymbol{\phi}) - f_{,\phi_\alpha}(\boldsymbol{\phi}, \mathbf{u}, \mathbf{m}) - \lambda.
\end{aligned}
$$

$\mathcal{L}$ refers to the integrand of Eq. (3.6), whereas τ on the left-hand side of Eq. (3.8) is a kinetic coefficient. The Langrange multiplier

$$
\lambda = \frac{1}{N} \sum_{\alpha=1}^{N} \xi (\nabla \cdot a_{,\nabla \phi_\alpha}(\boldsymbol{\phi}, \nabla \boldsymbol{\phi}) - a_{,\phi_\alpha}(\boldsymbol{\phi}, \nabla \boldsymbol{\phi})) - \frac{1}{\xi} w_{,\phi_\alpha}(\boldsymbol{\phi}) - f_{,\phi_\alpha}(\boldsymbol{\phi}, \mathbf{u}, \mathbf{m}),
$$

ensures the fulfillment of the conservation constraint Eq. (3.7). This can easily be seen by using the fact that Eq. (3.7) implies

$$
\sum_{\alpha=1}^{N} \frac{\partial \phi_\alpha}{\partial t} = 0,
$$

inserting the Eqs. (3.8) and solving for the parameter λ. For the gradient energy, we use the formulation

$$
(3.9) \qquad a(\boldsymbol{\phi}, \nabla \boldsymbol{\phi}) = \sum_{\alpha < \beta}^{N} \gamma_{\alpha\beta} |q_{\alpha\beta}|^2,
$$

where $q_{\alpha\beta} = \phi_\alpha \nabla \phi_\beta - \phi_\beta \nabla \phi_\alpha$ are generalized gradient vectors, and for the potential $w(\boldsymbol{\phi})$ a higher-order variant of a multi-obstacle potential is chosen (see [29]):

$$
w(\phi) = \begin{cases} \dfrac{16}{\pi^2} \displaystyle\sum_{\alpha < \beta}^{N} \gamma_{\alpha\beta} \phi_\alpha \phi_\beta + \displaystyle\sum_{\alpha < \beta < \delta}^{N} \gamma_{\alpha\beta\delta} \phi_\alpha \phi_\beta \phi_\delta, & \text{if } \phi \in [0,1]^N \text{ and } \sum_\alpha \phi_\alpha \equiv 1, \\ \infty, & \text{otherwise.} \end{cases}
$$

For phases α and β, the parameters $\gamma_{\alpha\beta}$ are their interface free energy per unit area, where the coefficients $\gamma_{\alpha\beta\delta}$ suppress spurious third phases if chosen to be about ten times the maximal $\gamma_{\alpha\beta}$ value (see [16]).

The displacement field is evolved component-wise. For the i-th component of the elastic displacement field ($i = 1, 2, 3$), a damped wave equation (cf. [28]) is applied

$$(3.10) \quad \rho\frac{\partial^2 u_i}{\partial t^2} + \kappa\frac{\partial u_i}{\partial t} = -\frac{\delta\mathcal{F}}{\delta u_i} = -\nabla\cdot\left(\sum_{\alpha=1}^{N}\mathcal{C}^\alpha(\epsilon(\mathbf{u}) - \epsilon_0^\alpha(\mathbf{u}))\right)_{i,\cdot}$$

$$= \frac{1}{2}\sum_{j=1}^{3}\sum_{\alpha=1}^{N}\frac{\partial}{\partial x_j}\left(\frac{\partial}{\partial\frac{\partial u_i}{\partial x_j}}(\epsilon(\mathbf{u}) - \epsilon_0(\mathbf{m}))\mathcal{C}^\alpha(\epsilon(\mathbf{u}) - \epsilon_0(\mathbf{m}))\right),$$

where the right-hand side is given by the divergence of the i-th row of $\mathcal{C}^\alpha(\epsilon(\mathbf{u}) - \epsilon_0^\alpha(\mathbf{u}))$. To describe the time-spatial evolution of the vector field of spontaneous magnetization, we use the Landau–Lifshitz–Gilbert equation (cf. [30])

$$(3.11) \quad \frac{\partial\mathbf{m}}{\partial t} = -\frac{\gamma}{1 + \alpha_G^2}(\mathbf{m}\times\mathbf{H}_{\text{eff}} + \alpha_G\mathbf{m}\times(\mathbf{m}\times\mathbf{H}_{\text{eff}})),$$

where γ is the gyromagnetic ratio of the system, and α_G is a phenomenological damping constant. By $\mathbf{H}_{\text{eff}}$ the effective magnetic field is denoted. Equation (3.11) has two contributions: first, a conservative precessional Larmor term around $\mathbf{H}_{\text{eff}}$, and second, a dissipative phenomenological damping term. The first term creates a gyration of $\mathbf{m}$ around $\mathbf{H}_{\text{eff}}$, the second term moves $\mathbf{m}$ towards $\mathbf{H}_{\text{eff}}$. The norm conservation condition $|\mathbf{m}| = 1$ has to be respected during numerical integration of the system. The effective field $\mathbf{H}_{\text{eff}}$ is derived from the free energy $\mathcal{F}$ via variation with respect to the spontaneous magnetization (cf. [24]):

$$(3.12) \quad \mathbf{H}_{\text{eff}} = -\frac{1}{\mu_0 M_S}\frac{\delta\mathcal{F}(\boldsymbol{\phi}, \mathbf{u}, \mathbf{m})}{\delta\mathbf{m}}$$

$$= \mathbf{H}_{\text{ext}} + \mathbf{H}_{\text{demag}} + \mathbf{H}_{\text{exch}} + \mathbf{H}_{\text{aniso}} + \mathbf{H}_{\text{m-el}}.$$

The fields $\mathbf{H}_{\text{exch}} = \frac{2A_{\text{exch}}}{\mu_0 M_S}\Delta\mathbf{m}$ and $\mathbf{H}_{\text{aniso}} = \frac{2K_{\text{aniso}}}{\mu_0 M_S}\sum_{\alpha=1}^{N}h(\phi_\alpha)(\mathbf{m}\cdot\mathbf{p}^\alpha)\mathbf{p}^\alpha$ in Eq. (3.12) are the exchange field and the anisotropy field, respectively. As, according to Eq. (3.5), magnetostrictive contributions to $\mathbf{H}_{\text{m-el}}$ can only arise from $\epsilon_0^\alpha(\mathbf{m})$, we neglect the magneto-elastic field in the present study (see Sec. 3.2 and [27]).

3.4. Discretization and numerical solution schemes

The equations stated above are discretized on a finite difference grid. The domain under consideration is decomposed into n rectangular cells: $\text{cell}_1, \ldots, \text{cell}_n$

of equal size. Eqs. (3.8) and (3.10) are solved using an explicit forward Euler scheme, that can be well parallelized. To enhance the numerical stability, the displacement field $\mathbf{u}$ is discretized using staggered grids for the components of $\mathbf{u}$. This is realized so that the values of u_i in cell_k lie in the center of the face of the the cell in x_i-direction ($i = 1, 2, 3$). The spontaneous magnetization $\mathbf{m}$, though being a vector-valued function, is discretized collocated in the center of the cells, as well as all other occuring quantities. We assume $\mathbf{m}$ to be piece-wise constant on each of the cells, i.e. $\mathbf{m}_{|\text{cell}_k} \equiv c_k \in \mathbb{S}^2$. This permits the interpretation of $\mathbf{m}$ as a volume averaged quantity in each cell. Assuming a finite sample in a non-magnetized environment, we can apply partial integration and the divergence theorem to rewrite the demagnetization field since the discrete convolution of a distance vector-dependent, symmetric second-order tensor-valued function N with the magnetization, and the volume averaged contribution of $\mathbf{H}_{\text{demag}}$ in cell_i is given as

$$(3.13) \qquad (\mathbf{H}_{\text{demag}})_{|\text{cell}_i} = -\sum_{j=1}^{n} N(r_i - r_j)\mathbf{m}_{|\text{cell}_j},$$

where r_k is the vector to the center of cell_k. This approach and interpretation follow [24]. The tensor N which depends only on difference vectors, reflects the (finitely extended) geometry of Ω, see [31] for a detailed derivation of N and its properties. As the formulation in Eq. (3.13) is a discrete convolution, it is possible to apply spectral methods like Fast Fourier Transform (FFT) to significantly speed up the computation, where further optimization is possible by exploiting the properties of N. Assuming the size of the simulated area of the sample to be much smaller than the size of the whole sample, one can interpret the simulation area as a representative volume element (RVE). This allows the usage of periodic boundary conditions for the magnetization. It is then adequate to solve for the scalar potential ψ in $\mathbf{H}_{\text{demag}} = -\nabla\psi$ in $\mathbb{R}^3$ directly in the Fourier space, where it reads

$$\hat{\psi}(k) = -iM_S \frac{\hat{m}_1(k)k_1 + \hat{m}_2(k)k_2 + \hat{m}_3(k)k_3}{|k|^2}.$$

The hat symbol $\hat{\ }$ denotes a Fourier transform, and the wanted solution can be obtained via inverse Fourier transformations. Eq. (3.11) is solved using geometric integration methods that are based on Lie-group theory, so the integration scheme is unconditionally conservative and first-order accurate. So, $\mathbf{m}$ evolves on the unit sphere without explicit renormalization. The basic idea of the scheme is to rewrite Eq. (3.11) in terms of a transitive Lie-group action on the configuration manifold of the system. For details on geometric integration look in [32], for the applied method and drawbacks of explicit renormalization, see [23]. The full elastic subproblem is respected by solving the wave equation Eq. (3.10). For

convenience, the commonly used Voigt notation can be adopted, where the symmetric fourth-order tensors have representations as symmetric real 6×6 matrices, and the second-order tensors as 6-component vectors. The notation simplifies the implementation and decreases the computation time. We remark that on transformation of the tensor quantities, what would be necessary for rotations of the frame of reference, one has to go back to the original tensor description.

4. Simulation setup and results

A set of simulations were performed to study the evolution dynamics and transition pathways of the martensite rearrangement process in Ni$_2$MnGa and to compare steady-state results to those predicted by the theory and experiment. As simulation domains rectangular 3D boxes with a regular grid were chosen and the evolution of all three components of the magnetization **m** and displacement vector **u** were calculated. For the sake of computation time, mostly quasi 1D or 2D setups were used (in which the magnetization and the elastic displacement field are still allowed to evolve in all three spatial dimensions), for which in the respective dimension only 3 grid layers were present. For the field **u**, either fixed displacements or stresses (surface tractions) were applied at the boundaries; for the magnetization either the special Neumann condition $\partial\mathbf{m}/\partial\mathbf{n} = 0$ or periodic boundaries were assumed, as given below for the specific cases.

4.1. Parameter set for Ni$_2$MnGa

The MSME problem includes twin and magnetic domains with dimensions and interfaces spanning different length scales, which have to be taken into account carefully when choosing the suitable parameter set. For the magnetic properties of the material Ni$_2$MnGa, the saturation magnetization of $6.015\cdot10^5$ A/m and the magnetocrystalline anisotropy constant of $2.45\cdot10^5$ J/m^3 were taken from reference [33], the exchange constant was chosen as $2\cdot10^{-11}$ J/m ([12]). A typical transition scale for the magnetic domains, which has to be resolved on the numerical grid, is the Bloch wall width of $\delta = \sqrt{A_{\mathrm{exch}}/K_{\mathrm{aniso}}} = 9\cdot10^{-9}$ m. Hence, we choose the physical grid distance to be $\Delta x = 2$ nm. This results in a simulation domain of 1 μm × 1 μm at 500 grid points resolution as a typical physical size of the simulated material volume. In Eq. (3.11) for the magnetization evolution, we assume, as proposed in [14], a gyromagnetic ratio of $\gamma = 2.21\cdot10^5$ m/As and a damping factor of $\alpha = 0.5$.

To treat the elastic problem in Ni$_2$MnGa, the mass density of $\rho = 8.02$ g/cm^3 is used from reference [33]. The tetragonal elastic stiffness tensor of the martensite variants is approximated by an averaged cubic tensor with values given in [34] (see Table 2), so that we can assume cubic symmetry in the solution

Table 1. Magnetic parameters for Ni$_2$MnGa, which were used in the simulation of twin boundary motion, including values nondimensionalized, using length and time scale d_0 and $t_0 = 1/\gamma M_s$ and the energy scale $f_0 = \mu_0 M_s^2$, with $\mu_0 = 4\pi \cdot 10^{-7}$ being the permeability of vaccuum.

quantity	M_S	K_{aniso}	A_{exch}	γ
SI units	[A/m]	[J/m^3]	[J/m]	[m/As]
	$6.02 \cdot 10^5$	$2.45 \cdot 10^5$	$2 \cdot 10^{-11}$	$2.21 \cdot 10^5$
nondim	1.0	0.539	11.0	1694

Table 2. Elastic and twin interface parameters for Ni$_2$MnGa, including dimensionless values.

quantity	ρ	c_{11}	c_{12}	c_{44}	γ_{twb}
SI units	[g/cm^3]	[J/m^3]	[J/m^3]	[J/m^3]	[J/m^2]
	8.02	$1.60 \cdot 10^{11}$	$1.52 \cdot 10^{11}$	$0.43 \cdot 10^{11}$	0.018
nondim	1694	$3.519 \cdot 10^5$	$3.343 \cdot 10^5$	$0.946 \cdot 10^5$	20

of the elastic equation (3.10). The data for the tetragonal martensite variant given in [13] were taken for the transformation strain, where only the diagonal components have nonzero values of $\alpha = 0.01$ and $\beta = -0.02$ (cf. Eqs. (2.2)). In Tables 1 and 2, the physical parameters are collected and supplemented by their nondimensional values, which were used throughout all simulations. For nondimensionalizing of the equations, spatial coordinates are expressed by $r = \tilde{r} \, d_0$ with a length scale $d_0 = 2$ nm and time as $t = \tilde{t} \frac{1}{\gamma M_s} = \tilde{t} \, t_0$ with $t_0 = 7.34 \cdot 10^{-12}$ s (all dimensionless quantities are indicated by a tilde and all scaling factors by a zero subscript). Together with a typical magnetostatic energy scale $f_0 = \mu_0 M_s^2 = 4.55 \cdot 10^5$ J/m^3, all bulk energy terms in the functional Eq. (3.6) can be written dimensionless. From the relation between magnetic field and energy (see Eq. (3.12)), the magnetic field scaling factor is then fixed as $H_{\text{eff},0} = M_s$. Additionally, for the interface tension of the twin boundary in the phase-field equation (3.8), a value of $\gamma_{\alpha\beta} = \gamma_{twb} = 0.018$ J/m^2 is assumed for each interface α/β (cf. Eq. 3.9). This value is more than two orders of magnitude smaller as compared to typical grain boundary interfacial tensions. This value is not well defined in the literature, but it can in principle be calculated from the atomic variant structure by ab initio methods. The diffuse interface width for the phase fields was taken (slightly smaller than the magnetic transition width) as $\xi = 3 \, d_0$, resulting in a resolution of about 8 grid points on the numerical grid. In the simulations, the kinetic coefficient in Eq. (3.8) was set to $\tilde{\tau} = 1$, so that $\tau = \tau_0 = f_0 t_0 / d_0$. Here we expect that the interface velocity is not significantly modified by the order parameter evolution, but is dominated by the

kinetics of strain propagation and magnetic evolution. For the case of elasticity, the time evolution is related to material density, elastic coeffcients and the damping coefficient in the wave equation (3.10), for which a value of $\tilde{\kappa} = 500$ was chosen.

4.2. Strain accommodation

For the examination of stress-field configurations, Ni_2MnGa magnetic shape memory alloy single crystals are typically operated under compressive stress, along one of the variants c-axes and under an external magnetic field in the perpendicular direction. As the martensite variant with the short c-axis along the direction of compression minimizes the elastic energy, and a second variant with this direction oriented along the external field minimizes the magnetic energy, a two-variant state is favored.

As a first test case, the reaction of a quasi one-dimensional system composed of two twin martensite variants (V_1 embedded in V_2, the index is representative for the Bain strain given in Eqs. (2.2)) was studied, where only the elastic energy was taken into account. Each variant extends over exactly one half of the box length (**x**-direction, grid chosen as $200 \times 10 \times 3$), as displayed in Fig. 3a, and periodic boundaries are applied for the phase fields. Initially, fixed normal displacements representing different total strains are prescribed at the **x**-boundaries and the elastic displacements relaxed to a stationary state, while not allowing the variant structure to change. Constant zero surface-traction boundary condi-
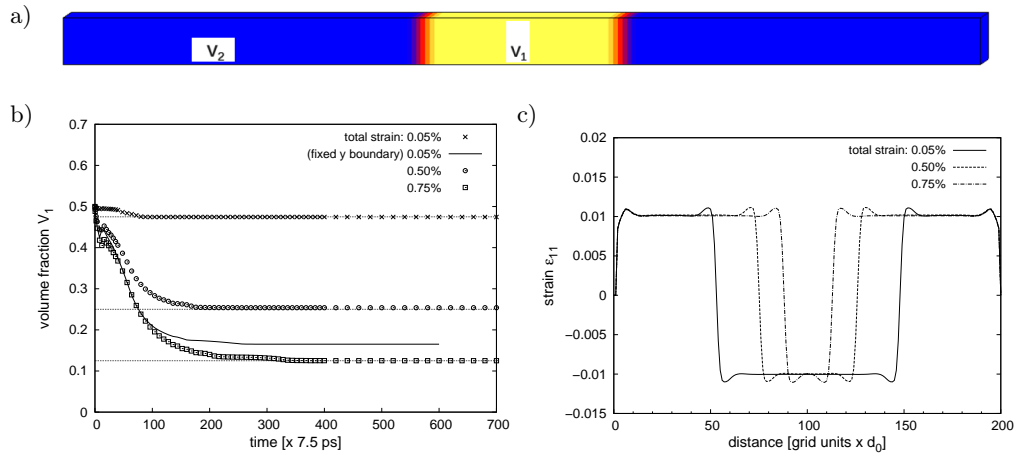

Fig. 3. a) Schematic setup of the 1D two-variant structure, with periodic boundaries in all directions for phase fields. b) Time evolution of volume fraction of variant V_1 under tensile load. The transformation produces a positive net strain to accomodate the preimposed external strain. c) Strain component profile $\epsilon_{11}(x)$ for the simulations from a).

tions were applied at the other two long boundaries. At simulation time $t = 0$ the phase-field evolution was started. The martensite variant V_1 with the short c-axis along the **x**-direction starts to shrink, in order to accommodate the externally imposed tensile strain, whereas the contrary effect can be observed under compression. Fig. 3b shows the temporal evolution of the volume fraction of V_1 for different values of total external strain, always leading to a stationary fraction of V_1. The resulting strain profiles in the long direction, ϵ_{11}, are given in Fig. 3c. The net difference in longitudinal strain between the two variants is in each case $\Delta\epsilon_{11} = 0.02$. To minimize the elastic energy in the system under a given strain, always the amount ζ of V_1 is transformed to V_2, which accomodates the total strain, $\epsilon_{11}^{\text{total}} = \zeta\Delta\epsilon_{11}$. In Fig. 3b the respective fractions ζ are given as horizontal dotted lines. When the elastic boundary condition for one of the long sides is changed, and instead of a stress-free boundary, the normal component of the displacement is fixed ($\partial\mathbf{u}/\partial\mathbf{n} = 0$), a much higher volume fraction is transformed to bear the tensile strain (solid curve in Fig. 3b for $\Delta\epsilon_{11} = 0.05$).

4.3. Coupled magneto-elastic simulations

We set up numerical simulations to analyze the coupled evolution of magnetic and elastic energies to elucidate the effect of magnetization for the system evolution. This work has the objective of finding general aspects in the mutual interaction of magnetic domains and twins. The physical relevant evolution path would include the growth of martensite platelets into the undercooled austenite phase with a preexisting magnetic domain structure, a topic which will be explored in future. The material parameters motivated in Sec. 4.1 were used and a grid size of $256 \times 256 \times 1$ was chosen. The inital configuration is shown in Fig. 4: a variant V_2 (yellow, c-axis along the **y**-direction) was embedded in a variant V_1 (blue, c-axis along the **x**-direction). The light and dark areas mark magnetic domains in which the local magnetization is aligned parallel or anti-parallel to a variants c-axis, respectively. No displacement along the **x**-direction was allowed (clamped boundary condition), while the other boundaries were kept stress-free. The magnetic boundary conditions are periodic and no external magnetic field was present. Two simulations were carried out, one with an initial magnetization providing $180°$ domain walls in direction of the **x**/**y**-bisector (see Fig. 4a), the other with an initially random magnetization (see Fig. 4d). In both cases, the vertical twin boundaries break up into facets along the [110] cubic (austenite) directions to minimize the elastic energy (as discussed in Sec. 2.2), and the evolution of $180°$ domain walls within the two variants can be observed. In the case of the initially random magnetization, more $180°$ domain walls develop during the early stage of the simulation, clearly effecting the evolution of the [110] facets, as the domain walls within variant V_2 are related to the 'kinks' variant V_2 develops.
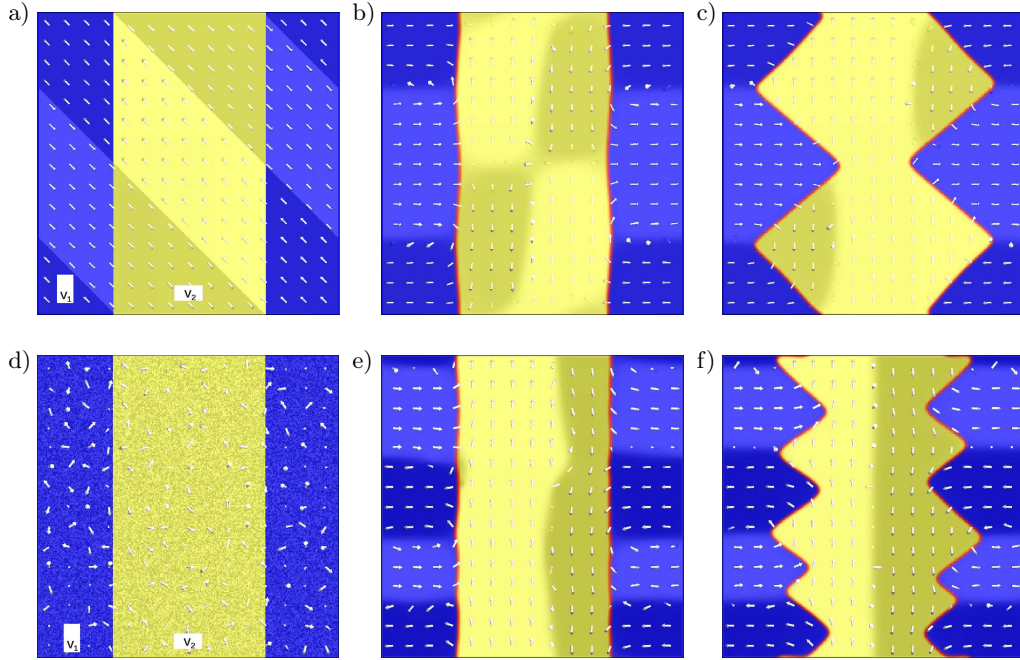
Fig. 4. Competitive development of coupled magneto-elastic variant and magnetic domain wall evolution under different inital magnetization states. The color scheme shows variant V_1 in blue and variant V_2 in yellow. The shading indicates the projection of $\mathbf{m}$ onto the easy axis of the variants: moments aligned parallel with the easy axis of the local variant are plotted lighter and moments aligned anti-parallel are plotted darker. The $90°$ domain walls coincide with the twin interfaces. In addition, the arrows shown indicate the direction of the magnetization. The simulation time is $\tilde{t} = 0$ in a) and d), $\tilde{t} = 96$ in b) and e) and $\tilde{t} = 2620$ in c) and f). The late state structures, as well as the developing volume fractions of the variants, differ significantly.

This effect is demanded by the minimization of the demagnetization energy, as $90°$ head-to-head or tail-to-tail domain walls are energetically unfavorable. These completely vanish during the evolution, so that all remaining $90°$ domain walls are head-to-tail. The final microstructures arangements are different, as distinctively different transition pathways are followed from the initial state.

4.4. Magnetically induced twin boundary motion

The field-induced rearrangement of twin microstructure as the basis of the MSME is studied in a simplified configuration. Quasi 2D simulations of two martensitic variants with the (110) twin planes, as in the material samples and a grid size of $100 \times 100 \times 3$, were carried out. The full magneto-elastic problem was solved here. The normal component of the displacement field is fixed to 0 at all boundaries, whereas the other components may evolve. For magnetization and phase fields, special Neumann boundary conditions ($\partial \mathbf{m}/\partial \mathbf{n} = 0$,
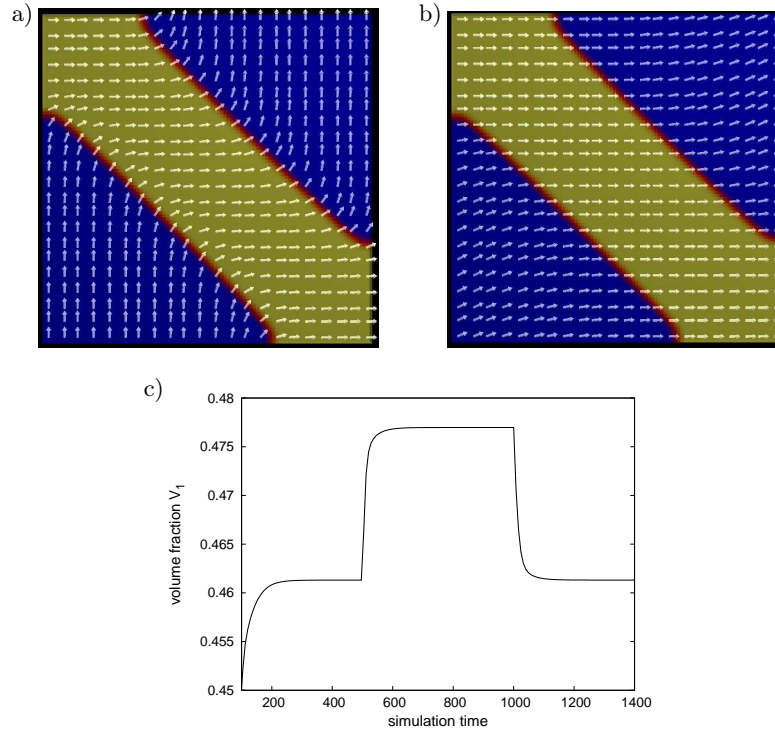
Fig. 5. Simulation of twin boundary motion induced by an external applied magnetic field. a) Initial relaxed 2D laminar microstructure. The arrows show the directions of the magnetization that follow clearly the easy axes of the variants. No other magnetic domain walls occur within the martensites. b) The resulting structure with an applied external magnetic field. Variant V_1 with the c-axis aligned along the field direction is energetically favored and grows. c) Plot of the development of the volume fraction of V_1 during the the field application cycle.

$\partial\phi_\alpha/\partial\mathbf{n} = 0$) were applied. First, the initial structure was relaxed, to reach a steady state configuration. Second, an external magnetic field of 1.5 Tesla was applied in the $\mathbf{x}$-direction, favoring the growth of variant V_1. After the steady state was reached, the external field was switched off in a third stage. During this evolution, the volume fraction of V_1 was reduced (see Fig. 5c). The application of the external field increases the Zeeman energy in the system, and due to its direction, V_1 grows to the detriment of V_2, resulting in an increase of stress at the domain boundaries. The recoverage of variant volume after turning off the field is complete, no hysteresis effects are observed.

4.5. Three variants state in 3D

The simple laminar configuration consisting of two martensitic variants V_1 and V_2 in 2D was extended in the $\mathbf{z}$-direction for a cubic 3D domain of grid size

$320 \times 320 \times 320$. The third martensitic variant V_3, having its short tetragonal c-axis along $\mathbf{z}$ orthogonal to those of the other two variants, was placed atop at about $2/3$ of the height of the simulation box. Compressive stress of 1.13 MPa (via surface traction boundaries) was applied along the $\mathbf{x}$- and $\mathbf{y}$-directions, which are the directions of the long crystal axes of variant V_3.
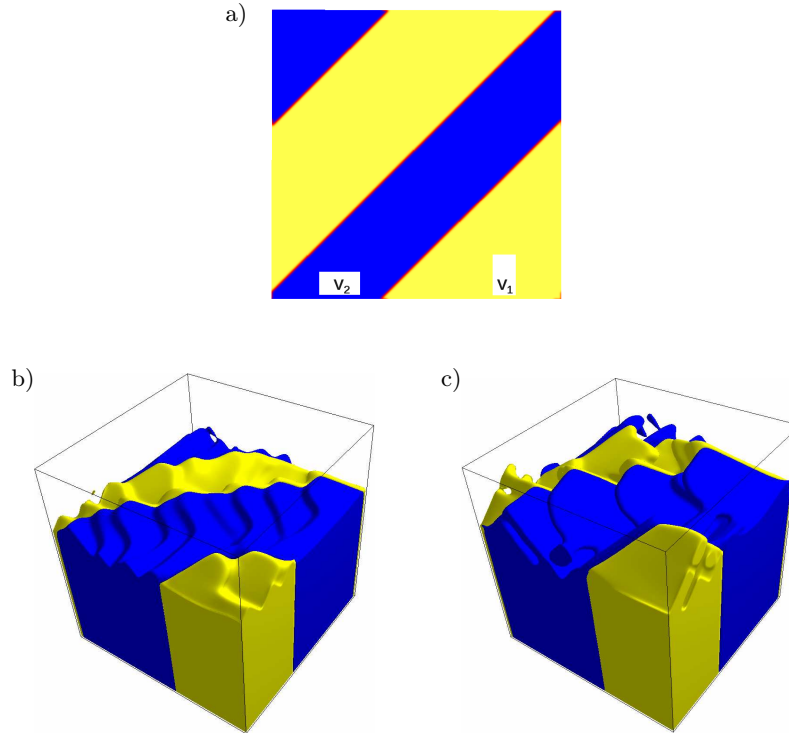

Fig. 6. Simulation of three different martensitic variants in 3D. a) Initial laminar setting on which a third variant V_3 is set atop, with tetragonal c-axis orthogonal to those of the shown variants. The third variant is not shown here. b) Plot of isosurfaces $\phi_{V_1} = 0.5$ and $\phi_{V_2} = 0.5$ in an early stage of the evolution process, where facets start to form. c) Final stage of the evolution before the top boundary of the simulation box is reached. The developed (110) facets can be observed.

The initial magnetization was set parallel to the $\langle 111 \rangle$ diagonal. Periodic boundary conditions for the magnetization were used, for the phase field parameters periodic boundaries in the $\mathbf{x}$-$\mathbf{y}$-plane and special Neumann boundary conditions in the out-of-plane dimension were applied. Because of the computational complexity of this simulation, the demagnetization energy was neglected here, underlining that this simulation is a test to show the general aplicability of the methods presented here. In Fig. 6b and 6c the isosurfaces of

the phase fields of V_1 and V_2 at an intermediate value of the order parameter, $\phi_{V_1} = 0.5$ in yellow and $\phi_{V_2} = 0.5$ in blue, are shown for an early and a later timestep (the magnetic domain structure is not shown). During the evolution, an intricate interface between the V_1–V_2 laminate and the third variant forms, consists of zig-zag shape arrangements of (110) facets as shown in Fig. 6b. As expected, V_3 dissolves and completely vanishes. In the later stage, twinned platelets grow into V_3, starting from the edges of the roof-like V_1–V_2 twin laminate surface.

5. Conclusions and outlook

We have proposed a general MSME phase-field approach to model magnetic field induced rearrangement of martensitic microstructure by the motion of twin boundaries. The model is based on a free energy formalism, taking into account local contributions from twin interfaces (interface, elastic and magnetic energies) and nonlocal contributions from magnetostatics and elastics. The numerical simulations demonstrate that the coupled system of magnetic and magneto-elastic equations lead to results that are at least in qualitative agreement with theoretical results. First steps towards the simulation of 3D scenarios are taken.

There are still limiting factors that prohibit simulations necessary for treating the representative material volumes. Due to the need to resolve the magnetic domain walls properly (that range around 17 nm for Ni-Mn-Ga based MSMAs, depending on the composition, see [10] and references therein), the overall size of the samples that can be simulated, is restricted to a range of microns, mostly due to memory limitations. Further, the demagnetization field computations are still complex, and even being lifted to Fourier space they remain time consuming.

Attempts are made to improve the numerical treatment by applying a parallel version of the FFT algorithm solving for the demagnetizing field, and the exploitation of the structure of the demagnetizing tensor. For the demagnetization field, appropriate boundary conditions to account for the surrounding domain structure of the simulated volume element, have to be formulated. The influence of interface thickness ξ and twin boundary energy γ_{twb} in the phase-field model will be examined, which are related to the topics of martensite nucleation and the quantitative verification of interface excess energy. The modelling of the martensitic rearrangement process for polycrystalline materials is important for many technical applications. In a future paper in preparation, we will extend our model to take into account differently oriented crystal grains hosting the martensite variants, separated by grain boundaries.

References

1. K. ULLAKKO, J.K. HUANG, C. KANTNER, R.C. O'HANDLEY, V. V. KOKORIN, *Large magnetic-field-induced strains in Ni₂MnGa single crystals*, Appl. Phys. Lett., **69**, 1966–1968, 1996.

2. S.J. MURRAY, M. MARIONI, S.M. ALLEN, R.C. O'HANDLEY, *6% magnetic-field induced strain by twin-boundary motion in ferromagnetic* Ni-Mn-Ga, Appl. Phys. Lett., **77**, 886–888, 2000.

3. A. SOZINOV, A.A. LIKHACHEV, N. LANSKA, K. ULLAKKO, *Giant magnetic-field-induced strain in* Ni-Mn-Ga *seven-layered martensitic phase*, Appl. Phys. Lett., **80**, 1746–1748, 2002.

4. K. OTSUKA, C.M. WAYMAN [Eds.], *Shape Memory Materials*, Cambridge University Press, 1998.

5. M.L. RICHARD, J. FEUCHTWANGER, S.M. ALLEN, R.C. O'HANDLEY, P. LÁZPITA, J.M. BARANDIARAN, *Martensite transformation in* Ni-Mn-Ga *ferromagnetic shape-memory alloys*, Metall. Mater. Trans. A, **38**, 777–780, 2007.

6. P. ENTEL, V.D. BUCHELNIKOV, M.E. GRUNER, A. HUCHT, V.V. KHOVAILO, S.K. NAYAK, N.A. ZAYAK, *Shape memory alloys: A summary of recent achievements*, Mater. Sci. Forum, **583**, 21–41, 2008.

7. K. BHATTACHARYA, *Comparison of the geometrically nonlinear and linear theories of martensitic transformation*, Continuum Mech. Therm., **5**, 3, 205–242, 1993.

8. A. DESIMONE, R. D. JAMES, *A constrained theory of magnetoelasticity*, J. Mech. Phys. Solids, **50**, 283–320, 2002.

9. K. BHATTACHARYA, *Microstructure of Martensite – Why it Forms and How it Gives Rise to the Shape-Memory Effect*, Oxford University Press, 2003.

10. V.C. SOLOMON, M.R. MCCARTNEY, D.J. SMITH, J. TANG, A.E. BERKOWITZ, R.C. O'HANDLEY, *Magnetic domain configurations in spark-eroded ferromagnetic shape memory* Ni-Mn-Ga *particles*, Appl. Phys. Lett., **86**, 192503, 2005.

11. J.X. ZHANG, L.Q. CHEN, *Phase-field model for ferromagnetic shape-memory alloys*, Phil. Mag. Lett., **85**, 531–541, 2005.

12. J.X. ZHANG, L.Q. CHEN, *Phase-field microelasticity theory and micromagnetic simulations of domain structures in giant magnetostrictive materials*, Acta Mater., **53**, 2845–2855, 2005.

13. Y.M. JIN, *Domain microstructure in magnetic shape memory alloys: Phase-field model and simulation*, Acta Mater., **57**, 2488–2495, 2009.

14. L.J. LI, J.Y. LI, Y.C. SHU, H.Z. CHEN, J.H. YEN, *Magnetoelastic domains and magnetic field-induced strains in ferromagnetic shape memory alloys by phase-field simulation*, Appl. Phys. Lett., **92**, 172504, 2008.

15. L.J. LI, C.H. LEI, Y.C. SHU, J.Y. LI, *Phase-field simulation of magnetoelastic couplings in ferromagnetic shape memory alloys*, Acta Mater., **59**, 2648–2655, 2011.

16. B. NESTLER, H. GARCKE, B. STINNER, *Multicomponent alloy solidification: Phase-field modelling and simulations*, Phys. Rev. E, **71**, 041609, 2005.

17. A. PLANES, L. MANOSA, A. SAXENA, *Magnetism and Structure in Functional Materials*, Springer, 2006.

18. H. GARCKE, B. NESTLER, B. STOTH, *On anisotropic order parameter models for multiphase systems and their sharp interface limits*, Physica D, **115**, 87–108, 1998.

19. W.F. BROWN JR., *Micromagnetics*, Interscience Publisher, 1963.

20. R. PHILLIPS, *Crystals, Defects and Microstructure: Modeling across Scales*, Cambridge University Press, 2000.

21. A. AHARONI, *Introduction to the Theory of Ferromagnetism*, Oxford Science Publication, 2000.

22. H. KRONMÜLLER, *General Micromagnetic Theory*, [in:] *Handbook of Magnetism and Advanced Magnetic Materials*, H. KRONMÜLLER, S. PARKIN [Eds.], John Wiley and Sons, 2007.

23. D. LEWIS, N. NIGAM, *A geometric integration algorithm with applications to micromagnetism*, J. Comput. Appl. Math., **151**, 141–170, 2003.

24. J.E. MILTAT, M.J. DONAHUE, *Numerical Micromagnetics: Finite Difference Methods*, [in:] *Handbook of Magnetism and Advanced Magnetic Materials*, H. KRONMÜLLER, S. PARKIN [Eds.], John Wiley and Sons, 2007.

25. J.D. JACKSON, *Classical Electrodynamics*, John Wiley and Sons, 1999.

26. R.E. NEWNHAM, *Properties of Materials: Anisotropy, Symmetry, Structure*, Oxford University Press, 2005.

27. O. HECZKO, *Determination of ordinary magnetostriction in* Ni-Mn-Ga *magnetic shape memory alloys*, J. Magn. Magn. Mater., **290**–**291**, 846–849, 2004.

28. R. SPATSCHEK, C. MÜLLER-GUGENBERGER, E. BRENER, B. NESTLER, *Phase-field modeling of fracture and stress induced phase transitions*, Phys. Rev. E, **75**, 066111, 2007.

29. F. WENDLER, C. MENNERICH, B. NESTLER, *A phase-field model for polycrystalline thin film growth*, J. Cryst. Growth, in press, 2011.

30. I. CIMRÁK, *A survey on the numerics and computations for the Landau–Lifshitz equation of micromagnetism*, Arch. Comput. Methods. Eng., **15**, 277–309, 2008.

31. A.J. NEWELL, W. WILLIAMS, D.J. DUNLOP, *A generalization of the demagnetizing tensor for nonuniform magnetization*, J. Geophys. Res., **98**, 9551–9555, 1993.

32. A. ISERLES, H.Z. MUNTHE-KAAS, S.P. NØRSETT, A. ZANNA, *Lie-Group Methods*, Cambridge University Press, 1999.

33. R. TICKLE, R.D. JAMES, *Magnetic and magnetomechanical properties of* Ni_2MnGa, J. Magn. Magn. Mater, **195**, 627–638, 1999.

34. P.P. WU, X.Q. MA, J.X. ZHANG, L.Q. CHEN, *Phase-field simulations of stress-strain behaviour in ferromagnetic shape memory alloy* Ni_2MnGa, J. Appl. Phys., **104**, 073906, 2008.